

Fabrication of Magnetic Fe₃O₄ Nanoparticles with Unidirectional Extension Pattern by a Facile and Eco-Friendly Microwave-Assisted Solvothermal Method

Ruey-Shin Juang^{1,2,3}, Chun-Ju Su⁴, Ming-Chung Wu^{1,5}, Hsi-Chuan Lu⁶,
Sea-Fue Wang⁶, and An-Cheng Sun^{4,*}

¹Department of Chemical and Materials Engineering, Chang Gung University, Guishan, Taoyuan 33302, Taiwan

²Division of Nephrology, Department of Internal Medicine, Chang Gung Memorial Hospital, Linkou 33302, Taiwan

³Department of Safety, Health and Environmental Engineering, Ming Chi University of Technology, Taishan, New Taipei City 24301, Taiwan

⁴Department of Chemical Engineering and Materials Science, Yuan Ze University, Chung-Li, 32003, Taiwan

⁵Division of Neonatology, Department of Pediatrics, Chang Gung Memorial Hospital, Linkou 33302, Taiwan

⁶Department of Materials and Mineral Resources Engineering, National Taipei University of Technology, Taipei 106, Taiwan

This study synthesizes iron(III) oxide magnetic nanoparticles (MNPs) using a facile and eco-friendly microwave-assisted solvothermal method. The highly porous particles become stable after a 60-min reaction when the temperature is fixed at 200 °C, in which the particle size is kept at 100–150 nm. The magnetic properties, crystal structure, surface morphology, and microstructures of the prepared MNPs are then analyzed. The microstructure analysis suggests that a MNP consists of numerous small Fe₃O₄ particles with a size smaller than 10 nm; therefore, a large amount of microcracks is observed between grains. Moreover, the orientations in these particles are very close, implying that they grow toward the same direction that may be provided by the nuclei. The prepared MNPs thus possess a highly porous structure and have a 3-times larger specific surface area than the commercially-available MNPs. Finally, the growth mechanism of iron(III) oxide MNPs by the present process is proposed.

Keywords: Fabrication, Magnetic, Fe₃O₄, Nanoparticles, Unidirectional Extension Pattern, Microwave-Assisted Solvothermal Method.

1. INTRODUCTION

Nanoscience is one of the most essential fields among modern sciences, which changes a great deal of our perception of technology, even our life. Nanomaterials possess many advantages due to their unique size dimension and physicochemical properties. Among the wide range of nanomaterials, magnetic nanoparticles (MNPs) have many special characteristics such as superparamagnetism, large surface-to-volume ratio, high magnetic susceptibility, etc. These characteristics dramatically increase the developed value of MNPs. MNPs have shown potential applications in several areas, including heterogeneous catalysis,^{1,2} adsorption,^{3,4} ferrofluids,^{5,6} magnetic resonance imaging (MRI),^{7–9} drug delivery,^{10,11} and cancer therapy (hyperthermia).^{12–14} Hence, MNPs are regarded as

novel materials in nanoscience. Recently, much attention has been attracted to and considerable efforts have been spent on the development of MNPs. The versatility of MNPs has spurred more and more clinical trials, advanced applications, and fundamental research including synthetic routes,^{15–34} surface modifications,^{11,14} property studies,^{35,36} and composite materials,^{1,37} which have been developed during the past decades.

Among all the applications, the biomedical field^{10–14,38–43} appears to be one of the most valued places, because the unparalleled characteristics of MNPs are difficult to be replaced by other known materials. Nanomagnetite particles possess several advantages including non-toxicity and excel bio-compatibility.^{38–40} Actually, the safety of iron(III) oxide MNPs has been investigated by Jain et al.^{39,41} The results of target drug delivery,^{10,11} hyperthermia,^{12–14} bio-label, and bio-sensing^{42,43} indicate

* Author to whom correspondence should be addressed.

that iron(III) oxide MNPs could improve current medical techniques. Therefore, iron(III) oxide MNPs are regarded as promising materials in medical treatment. Given the importance and development of iron(III) oxide MNPs, it is highly desired to build an effective and eco-friendly synthesis method.

A few methods have been reported to synthesize MNPs such as co-precipitation,^{15, 16} thermal decomposition,^{17, 18} microemulsion^{19, 20} hydrothermal,^{21–23} and solvothermal.^{24, 25} Other ways such as sol–gel,^{26, 27} sonochemical,^{28–30} chemical vapor deposition, and ball milling^{31, 32} have been also demonstrated. Although MNPs with a larger specific surface area could be obtained using some common synthesis methods, low magnetic performance and higher time consumption are the major drawbacks among these methods.^{44–48} For example, the hydrothermal method could synthesize MNPs with a specific surface area of 150–160 m²/g at a particle size of 300 nm; however, the procedures take over 24 h.^{44, 46, 47} Moreover, MNPs with a specific surface area of about 285 m²/g were obtained from the co-precipitation method at a particle size of 98 nm.⁴⁵ Such two-step synthesis processes with different reaction times and temperatures make the fabrication too complicated and out of control. From the practical perspective, a highly efficient way to fabricate MNPs without losing surface area is very important. It is known that microwave radiation is a great source of heat energy that offers a clean and effective form of heating. Thus, microwave was adopted to accelerate the synthesis process in this work.^{33, 34}

This study combines the solvothermal and microwave heating methods and calls it a microwave-assisted solvothermal method. The advantages include not only the saving of time and energy, but also benignancy to the environment since the process was carried out in a closed system and a strong acid/base was not involved in this process. This research optimizes the synthesis process by focusing on the effect of reaction time on the properties of MNPs. The fracture-like structure of Fe₃O₄ particles was observed. After comparing to commercially-available Fe₃O₄ particles with similar particle size, the specific surface area of our synthesized powders was about three times larger than that of the commercial one. The results of this study could offer a complete picture of the microwave-assisted solvothermal method and help analyze the physicochemical properties of the synthesized particles.

2. EXPERIMENTAL DETAILS

2.1. Materials

Iron(III) chloride (purity 97%) was supplied from Aldrich (St. Louis, MI, U.S.A.). Sodium acetate (purity 98%) was supplied from SHOWA Chemical Co. (Gyoda, Saitama, Japan). Ethylene glycol (purity >99%) was purchased from J.T. Baker (Corporate Parkway Center Valley, PA, U.S.A.). Polyethylene glycol (molecular weight,

20,000 g/mol) was offered from Alfa Aesar (Ward Hill, MA, U.S.A.). All chemicals were used as received without further purification. Commercially-available magnetic Fe₃O₄ nanoparticles with a particle size of 100–150 nm were purchased from Nanostructured and Amorphous Materials Inc. (Houston, TX, U.S.A.), which were also adopted for comparison in this work.

2.2. Synthesis of Magnetic Fe₃O₄ Particles

In this work, iron(III) chloride was used as a precursor to synthesize Fe₃O₄ MNPs, and ethylene glycol served as a reductant. Iron(III) chloride (1.08 g) was dissolved into 40 ml ethylene glycol in an 80-ml sample vial. Sodium acetate (4 g) and polyethylene glycol (1 g) were added into the solution with vigorous stirring. Afterwards, the well-mixed solution was put into the microwave reactor with a magnetic bar. The microwave reactor provides a rapid and uniform energy source to support the reaction, while ethylene glycol is a great agent to energy adsorption with a higher dielectric constant.

Experiments were conducted under varying reaction times, which were set at 5, 10, 15, 20, 30, 45, 60, 75, 90, and 105 min, and the temperature was fixed at 200 °C throughout the experiments. The result of this group shows the effect of reaction time on the properties of MNPs. After the reaction, the microwave system was cooled to room temperature. When the solution was cooled, the precipitates formed. The Nd-Fe-B magnets were used to separate magnetic precipitates and the solution. The magnetic precipitates were washed with ethanol and then dried at 65 °C. For those precipitates that are not attracted by the magnets, they were filtrated and separated from the solution with a 0.45- μ m membrane filter by suction. The precipitate was then dried at 65 °C, and the dried particles were stored for further analysis and use.

2.3. Characteristics of Magnetic Fe₃O₄ Particles

The functional groups of the particles were characterized through the Fourier transform infrared (FTIR) absorption spectroscopy (PerkinElmer Spectrum 100, Massachusetts, U.S.A.). Crystal structures of the powders were analyzed by D2 PHASER X-ray diffractometer, XRD (Bruker, Germany) with a scanning region of 2 θ from 10° to 70°. Chemical composition and bonding energy were characterized by the X-ray photoelectron spectroscopy, XPS (JSM-2010, Tokyo, Japan). The magnetic properties of the samples were measured by using a vibrating sample magnetometer, VSM (DMS model 1660, ADE Technologies Inc., MA, U.S.A.). The surface morphology of the MNPs prepared under various conditions was determined by JEOL scanning electron microscope, SEM (JSM-7800F Prime, Tokyo, Japan). The selected area electron diffractions (SAED) and microstructures of the powders were observed by a JEOL transmission electron microscope, TEM (JSM-2010, Tokyo, Japan) with accelerating voltage

at 200 keV. The BET specific surface areas of the samples were measured from the adsorption–desorption isotherms of N₂ at –196 °C using a porosimeter (ASAP2020, Micromeritics Instrument Co., GA, U.S.A.). Prior to measurement, the sample was dried overnight in an oven at 130 °C and then placed in the sample tube. After that, the tube was heated to 230 °C and evacuated for 4 h until the pressure was less than 1.3×10^{-7} bar. The total pore volumes of the MNPs were determined from the same adsorption–desorption isotherms stated above, according to the manufacturer’s software (based on the Kelvin equation), and the pore size distribution was derived from the BJH theory.⁴⁹

3. RESULTS AND DISCUSSION

3.1. Chemical Characteristics of the Synthesized Fe₃O₄ MNPs

Figure 1 presents the pictures of the reaction process with different reaction times. It is clear that the reaction seemed to finish at 60 min, because the solution consequently became more transparent and the color was black, which is totally different to those shown in Figures 1(a)–(c). The black particles precipitated and settled in the bottle. In order to realize the macro magnetic behavior of the synthesized particles, the Nd-Fe-B magnets were used to attract the precipitated particles. Figure 2 presents a picture of the MNPs (at 60 min) attracted by the Nd-Fe-B magnets. Obviously, the MNPs were fully attracted by the magnets, implying that the MNPs would be well controlled by the applied magnetic field. The magnetic properties of the MNPs were detected by VSM, and the results are shown in Figure 3. As the reaction time is less than 30 min, the powders present weak magnetism. The inset shows superparamagnetic properties of MNPs at 5 and 30 min, respectively. The saturation magnetization (M_s) is lower than 0.4 emu/g, suggesting that few MNPs are formed during the reaction. When the reaction time increased to 45 min, superparamagnetic MNPs with high M_s were found. Further extending the time just enhances M_s , implying that more MNPs are formed. It is noted that the highest M_s (~30 emu/g) was found at 60 min. The reaction appears to stop after 60 min, because M_s no longer increased with reaction time.

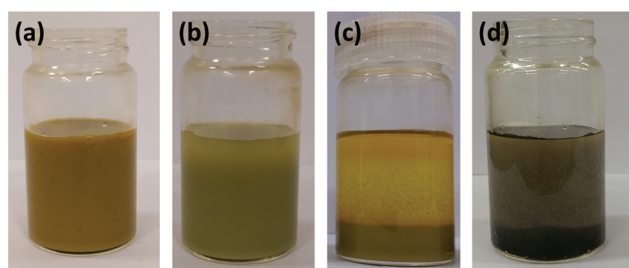


Figure 1. The pictures of the reaction processes within (a) 5, (b) 20, (c) 30, and (d) 60 min.

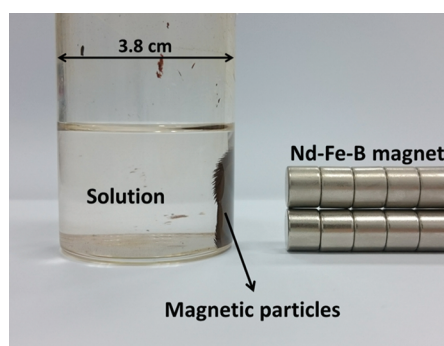


Figure 2. The picture of the MNPs attracted by the Nd-Fe-B magnets (outside applied magnetic field).

The functional groups of the prepared MNPs were analyzed with FTIR operating in a transmission mode from 4000 to 450 cm⁻¹. Figure 4 shows the FTIR spectra. The absorption peaks at 1627 cm⁻¹ and 3421 cm⁻¹ are indicated by the vibration of the OH group.¹¹ These peaks are attributed to water molecules in the air. In addition, the peaks of C–H (2880 cm⁻¹) and C–O (1050 cm⁻¹) groups are observed from the solution. However, Fe–O stretching vibrations are detected at 627 cm⁻¹.¹¹ The Fe–O absorption peak is clearer with increasing reaction time, which means that iron(III)-oxide magnetic particles form better under a longer time frame.

The crystal structure and phase purity of the MNPs were characterized by XRD measurements. Figure 5 shows the XRD patterns. The spectra obtained for reaction times of 45, 60, 75, and 90 min suggested that the crystal structure of the MNPs is a cubic Fe₃O₄ phase, because the peaks (220), (311), (400), (422), (511), and (440) are observed at 2θ values of 30.1°, 35.4°, 43.2°, 53.3°, 56.8°, and 62.4°, respectively, which agree with JCPDS No. 82-1533. Peaks with higher intensity obtained at more than 60 min suggest the existence of a more stable Fe₃O₄

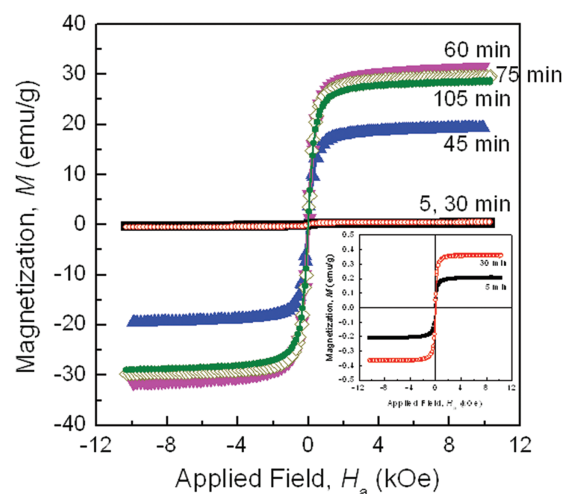


Figure 3. The magnetic properties of the MNPs reacted at 200 °C with different reaction times.

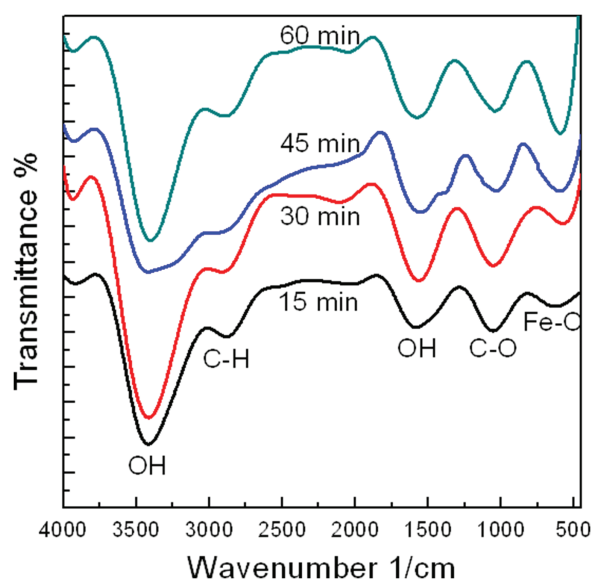


Figure 4. FTIR spectra of the MNPs reacted at 200 °C with different reaction times.

crystal phase. These results also suggested only a few amounts of Fe₃O₄ powders were synthesized if the reaction was shorter than 45 min. Moreover, according to the XRD patterns, we observed the formation of sodium chloride (NaCl) peaks (200) and (220) at 2θ values of 32° and 45°, respectively, which are consistent with the JCPDS No. 88-2300. This indicates that NaCl is formed in this process when the reaction is incomplete. However, NaCl peaks were not shown in the samples prepared at 45, 60, 75, and 90 min, because these MNPs were separated via an external magnetic field after the reaction. In other words, magnetic separation is an effective way to obtain pure magnetic particles. In addition, the average crystallite size (D) could be calculated using the Scherrer equation,^{11,50} $D = K\lambda/(\beta \cos \theta)$, where K is a constant ($=0.89$ for Cu- $K\alpha$), λ is wavelength ($=0.154$ nm for Cu- $K\alpha$), β is the full width at half maximum, and θ is the Bragg diffraction

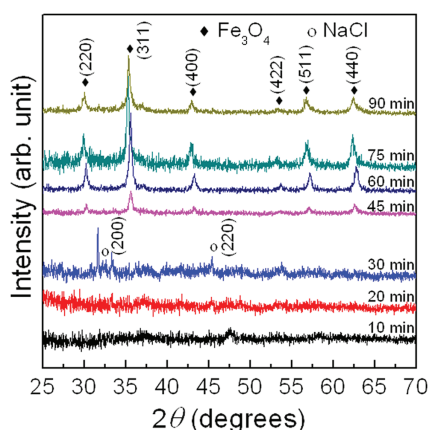


Figure 5. XRD patterns of the MNPs reacted at 200 °C with different reaction times.

angle. Therefore, we choose the case of the 60-min sample as an example to calculate the crystallite size, which was around 26.93 nm.

The XRD patterns of Fe₃O₄ and γ -Fe₂O₃ are similar. To further confirm the structures of these particles, X-ray photoelectron spectra (XPS) analysis can provide decisive evidence. The XPS spectra are shown in Figure 6. The peaks of binding energy around 710 eV and 725 eV are Fe 2p_{3/2} and Fe 2p_{1/2}, respectively. The results match well with the reported values of Fe₃O₄ in the literature.^{21,51} It is known that the binding energy of element increases with a greater valence state. The binding energy of Fe 2p_{3/2} is about 709 eV for Fe²⁺ and 711 eV for Fe³⁺. Figure 6 presents the XPS signals of the Fe 2p regions, and the peak of Fe 2p_{3/2} is at around 710 eV, which indicates that both Fe²⁺ and Fe³⁺ should exist showing the formation of Fe₃O₄. The peak that shifts from 710.5 eV at 30 min to 711.2 eV at 60 min is evidence that the highly oxide Fe₃O₄ phase is obtained after increasing the reaction time. This result confirms that the prepared particles are Fe₃O₄. It also suggests that Fe₃O₄ was synthesized at 30 min, although the XRD pattern does not show clear peaks of Fe₃O₄. This outcome is due to the rare number of the particles, which weakens the intensity of the peaks.

Figure 7 shows the SEM images of the synthesized particles with reaction time ranging from 5 to 105 min. From Figures 7(a) and (b), no particles are formed, but many flakes are obtained. As the reaction time increased to 30 min (see Fig. 7(c)), some particles with a size of 50 nm are deposited on the flakes, indicating the initial formation of Fe₃O₄ nanoparticles. This result has also been confirmed in the above magnetic hysteresis loop and XPS spectra. Figure 7(d) presents that large amounts of Fe₃O₄ nanoparticles were formed at 45 min. The particles size increases to about 200 nm. However, a few flakes were still observed in this picture; obviously, more time is still needed to finish the reaction. Further extending the reaction time to over 60 min makes the reaction complete, and the shape of the particles is much closer to the sphere

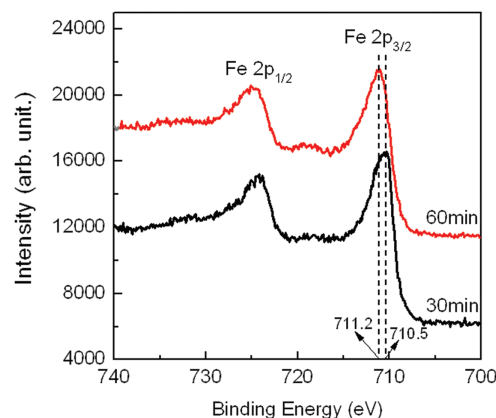


Figure 6. XPS spectra of the MNPs reacted at 200 °C within 30 and 60 min.

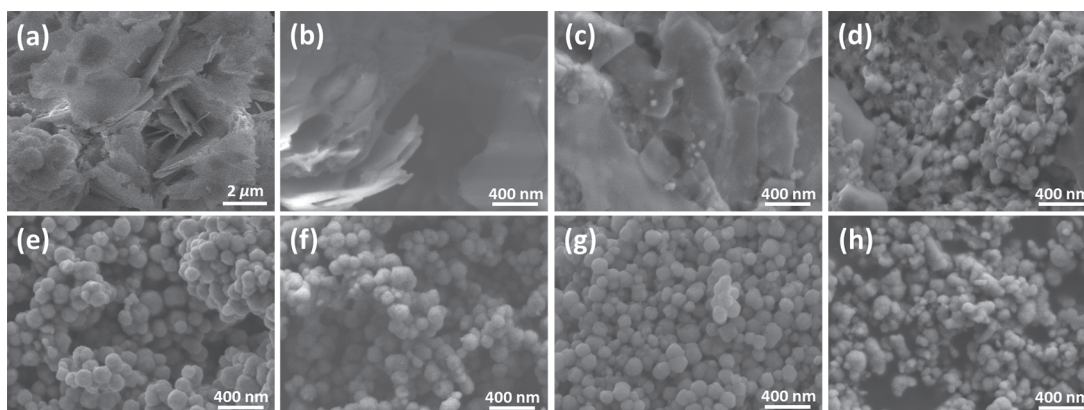


Figure 7. Surface morphologies of the MNPs reacted at 200 °C with different reaction times, where the reaction time is (a) 5, (b) 20, (c) 30, (d) 45, (e) 60, (f) 75, (g) 90, and (h) 105 min.

as shown in Figure 7(f). In this case, the flakes are no longer found. The particles size is kept constant at 100–150 nm as shown in Figures 7(g)–(h), even as the reaction time reaches 105 min. Those pictures obviously show the agglomeration of the particles, probably because the MNPs possess high surface area and strong dipole–dipole interactions. In general, the agglomeration of particles could decrease the large surface energy.

The microstructure of the MNPs was examined by TEM. Figures 8(a)–(f) show the bright field TEM images of the Fe₃O₄ particles obtained at various stages of reaction times. Figures 8(a)–(c) present the flake matrix structures, which are consistent with the SEM results, with particles found on the flakes. As the reaction time is longer than 45 min, the flake structures disappear and the particles gradually take spherical shape as shown in Figures 8(d)–(f). It is noted that numerous microcracks appears at the particle surface in each stage. It is believed that the large specific surface area will be obtained for these powders, because the cracks may provide extra surface area. Further extending the reaction time just makes the particles stable. The insets in Figures 8(a)–(c) are the corresponding electron diffraction patterns. The inverse *d*-spacing of the spots in these patterns is calculated to be 7.92, 9.52, 11.68, 12.34, and 13.50 nm⁻¹, which correspond to the Fe₃O₄ phases with (311), (400), (422), (511), and (440) planes, respectively. These results are also consistent with those reported in literature.⁵² The size of the MNPs measured by TEM increases with reaction time. In Figures 8(a)–(c), the size is about 50–60 nm when the reaction is shorter than 45 min and rises to 100–150 nm in Figures 8(d)–(f) when the reaction time is over 45 min. The results fully agree with those in Figures 7(d)–(h) when the reaction is longer than 45 min.

3.2. Magnetic Properties of the Synthesized Fe₃O₄ MNPs

From the aforementioned results, it is concluded that the reaction time can be longer than 45 min when the

temperature is at 200 °C during the microwave-assisted solvothermal process. To compare the physicochemical properties between the synthesized and commercially-available MNPs, Fe₃O₄ particles with a particle size ranging from 100–150 nm were purchased. Figure 9 presents the hysteresis loop, crystal structure, surface morphology, and microstructures of the purchased Fe₃O₄ nanoparticles. In Figure 9(a), the commercial particles show typical superparamagnetic property, which is similar to our synthesized ones. The inset in Figure 9(a) proves that the commercial MNPs are also cubic Fe₃O₄ crystals, because peaks (111), (220), (311), (400), (422), (511), and (440) are observed at 2θ values of 18.3°, 30.1°, 35.4°, 43.1°, 53.4°, 56.9°, and 62.5°, respectively. These findings agree with the synthesized MNPs. However, the M_s value is about 50 emu/g, increasing by 20 emu/g compared to the MNPs prepared at 60 min. It should be noted that the particle size of commercial Fe₃O₄ nanoparticles is 100–150 nm, and our synthesized MNPs at 60 min show the same size. The M_s value is calculated from the total magnetic moment (*M*) of a sample divided by the total weight of a sample. These two types of Fe₃O₄ MNPs have the same crystal structure, particle size distribution, and total sample weight, but different M_s values—that is, they both have different microstructures that affect the sample's total *M*.

The SEM picture (Fig. 9(b)) depicts that the commercial Fe₃O₄ nanoparticles have a well crystalline structure. The particles are crystalline with a cubic shape as shown in the inset of Figure 9(b), which is an enlarged picture from the dash-square region in Figure 9(c). They are typical cubic Fe₃O₄ crystal structures. The inner structures are obtained from the TEM measurements, and the results are presented in Figures 9(c) and (d). The particle size is between 100–150 nm in Figure 9(a), and the well crystalline can be identified by the clear defined grain boundary in the inset picture magnified from the dash-region in Figure 9(c). Although the commercial particles

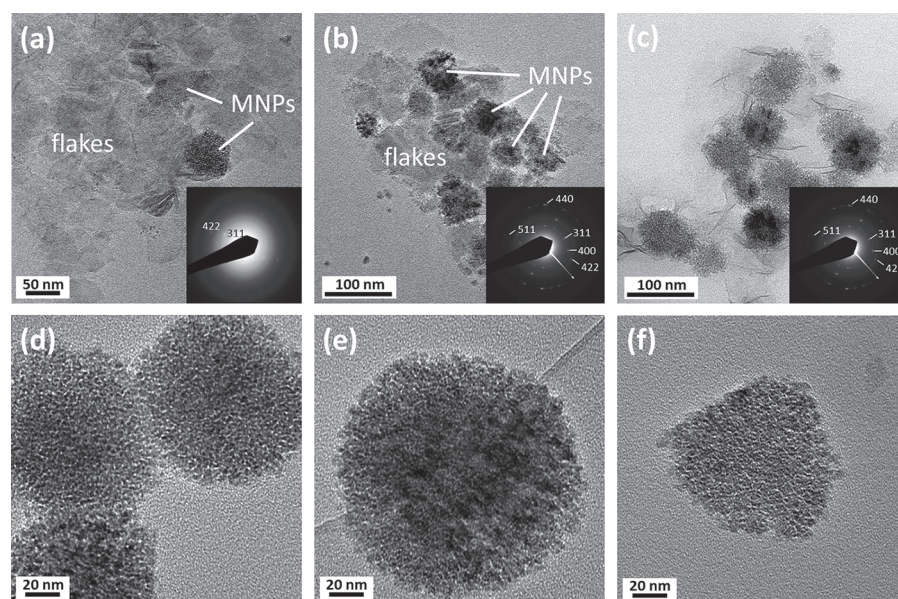


Figure 8. The bright-field TEM images of the MNPs reacted at 200 °C with different reaction times, where the reaction time is (a) 15, (b) 30, (c) 45, (d) 60, (e) 90, and (f) 105 min. The insets in (a)–(c) are the corresponding selected electron diffraction patterns.

present similar size to the synthesized ones with a reaction time larger than 45 min, the microstructures look fully different. Figure 9(d) is the large magnified TEM picture of one commercial Fe₃O₄ particle. Except for the 4 well defined boundaries, the inner structures in commercial Fe₃O₄ particles are solid; on the contrary, porous structures are observed in our prepared MNPs as shown in Figures 8(d)–(f). Although both the commercial and

synthesized Fe₃O₄ particles have the same crystal structure, particle size distribution, and total sample weight, the porous structure contributes to a lower magnetic moment than the solid structure. This may explain the lower M_s in the present synthesized MNPs.

3.3. Porous Properties of the Synthesized Fe₃O₄ MNPs

Through the microwave-assisted solvothermal method, we want to understand why highly porous Fe₃O₄ MNPs are synthesized at a particle size of 100–150 nm. The adsorption–desorption isotherms of N₂ gas on both commercial and synthesized Fe₃O₄ MNPs and the corresponding pore size distributions are shown in Figure 10. The isotherms for the prepared MNPs in this work are classified as type IV, which indicates the presence of mesopores. In addition, the hysteresis loops obtained in these cases are H3, which exhibit a narrow distribution associated with the cylindrical pores. The isotherm for the commercial Fe₃O₄ particles lacks hysteresis behavior. Our synthesized powders have a more specific surface area than the commercial one. The pore size distributions and pore sizes of commercial and synthesized Fe₃O₄ particles are plotted as the inset in Figure 10. It is clear that a narrow distribution at a size smaller than 100 nm is presented for commercial particles. A wider distribution is obtained for the synthesized particles, especially for the sample obtained at 45 min.

The specific surface area of MNPs was estimated by the BET method demonstrated in the inset in Figure 11. In a similar size scale, the surface area of commercial Fe₃O₄ particles is 9 m²/g, but those of the synthesized MNPs are 33, 30, 28, 26, and 21 m²/g at 45, 60, 75, 90, and 105 min, respectively. The surface area of all synthesized MNPs is larger than that of the commercial one, providing strong

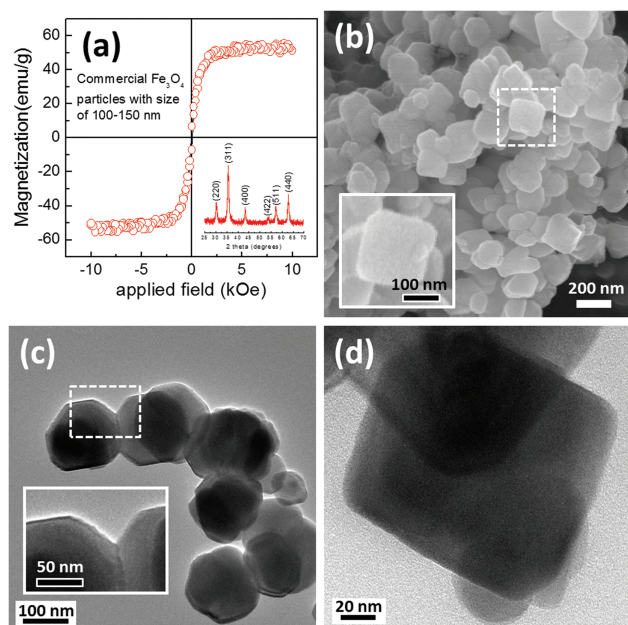


Figure 9. The (a) magnetic property, (b) surface morphology, (c) low magnified TEM bright field image, and (d) high magnified TEM bright field image of commercial Fe₃O₄ nanoparticles. The inset in (a) is the XRD pattern of commercial Fe₃O₄ nanoparticles. The insets in (b) and (c) are the enlarged pictures of dash square regions in (b) and (c).

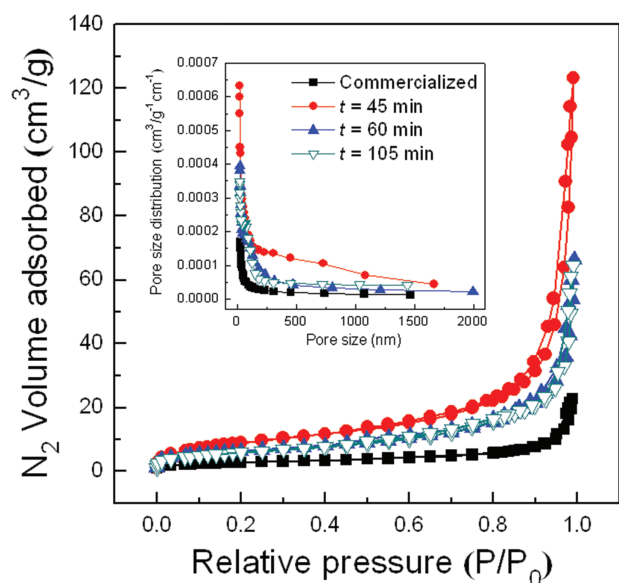


Figure 10. Adsorption–desorption isotherms of N₂ on commercial and synthesized MNPs with different reaction times. The inset is the pore size distribution curves of commercial and synthesized MNPs with different reaction times.

evidence toward the porous structure of the synthesized Fe₃O₄ in this study. The difference in surface area can explain why the TEM images demonstrate a porous sphere rather than a smooth one.

3.4. Microstructures of the Synthesized Fe₃O₄ MNPs

To further analyze the porous microstructure of synthesized Fe₃O₄ nanoparticles, the results of high resolution TEM analysis are presented in Figure 12. From Figure 12(a), it is obvious that a big and single Fe₃O₄ particle consists of numerous small Fe₃O₄ particles. Each particle is usually small than 10 nm, and thus a large amount of microcracks is observed between grains. The orientations in these particles are very close, implying that they

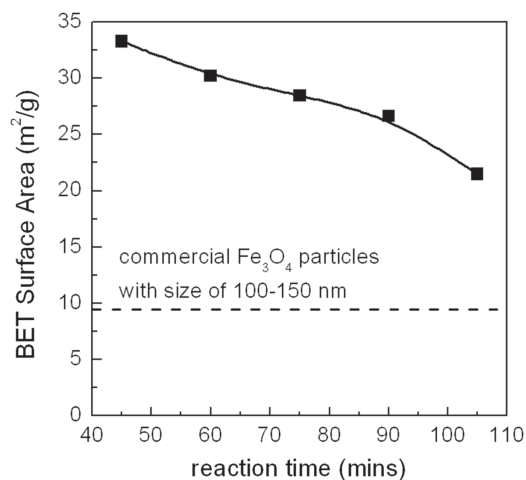


Figure 11. The BET specific surface area of commercial and synthesized MNPs with different reaction times.

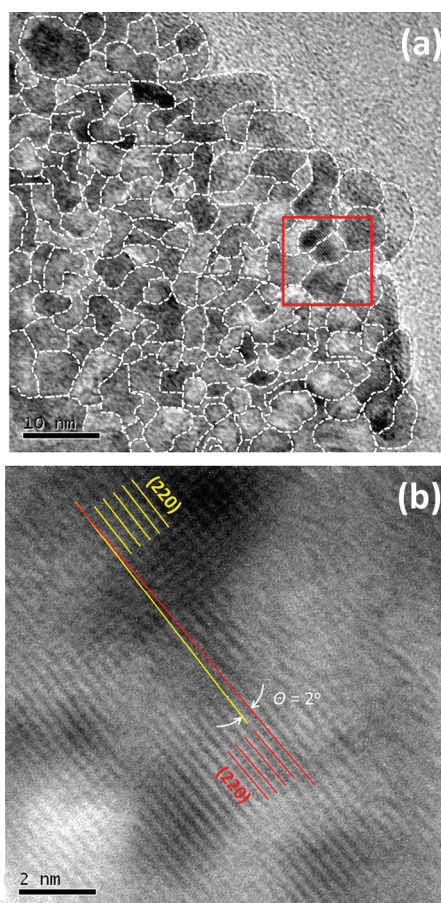


Figure 12. (a) High resolution TEM image and (b) lattice structure of synthesized MNPs (The reaction time of this sample is 105 min).

grow toward the same direction, which may be provided by the nuclei (the so-called unidirectional extension pattern). These results are consistent with those in adsorption–desorption isotherms of N₂. Figure 12(b) shows the lattice structures, which is the magnified image of the red square region in Figure 12(a). This demonstrates that a big synthesized Fe₃O₄ particle is well crystallized, which means that the synthesized process in this study can obtain highly crystallized MNPs. The Fe₃O₄ (220)-orient are found in the grains; however, $\theta = 2^\circ$ between the (220) planes reflects that these grains grow at any time. The big and single Fe₃O₄ particle is truly constructed by stacking the small Fe₃O₄ particles.

In order to highlight that many small Fe₃O₄ particles can construct a big and single porous Fe₃O₄ particle, the selected area electron diffractions (SAED) and TEM dark field technology were used and the pictures are shown in Figure 13. Figure 13(a) is the TEM bright field image of the synthesized Fe₃O₄ MNPs at 60 min. The particles are spherical, and the size is about 100–150 nm. The surface of these particles is rough, indicating that there is a porous structure inside them. The electron diffraction pattern of Figure 13(a) is depicted in Figure 13(b). Here, the (311), (400), (422), (511), and (440) crystal planes can be

identified. The (400) and (440) planes' diffraction spots are selected as the electron beam sources to get the TEM dark field images, as shown in Figures 13(c) and (d), respectively. Obviously, there are many small light dots in these two figures, proving that the particles truly have (400) and (440) orientations in Figures 13(c) and (d), respectively. These light particles are usually around 2 to 6 nm, and a vast number of them are assembled together and integrated to become a big Fe₃O₄ particle—that is, the large particles with a diameter of nearly 100–150 nm actually consist of many nanoparticles. Moreover, small particles like to crystallize in a similar direction. These results are in agreement with those shown in Figure 12. The formation of such a structure might be due to the tendency of reducing surface energy among the particles. Hence, the nanoparticles tend to congregate to lower their surface energy. It was also found that every particle is almost formed as a sphere structure, due to the fact that a sphere presents the minimum surface energy. The nucleus stacked in different planes on the surface of the nucleus is also confirmed from SAED images. It is also evidence that a rough surface and porous structure are formed for the synthesized Fe₃O₄ nanoparticles here. Therefore, they possess a notably high specific surface area.

From the above results, the growth mechanism of Fe₃O₄ nanoparticles by the present synthesis process was schematically proposed in Figure 14. At the beginning, the reductant ethylene glycol reduced the iron(III) chloride through absorbing the microwave energy. The Fe₃O₄ nucleus formed and got together in order to decrease the high surface energy. However, due to different crystal

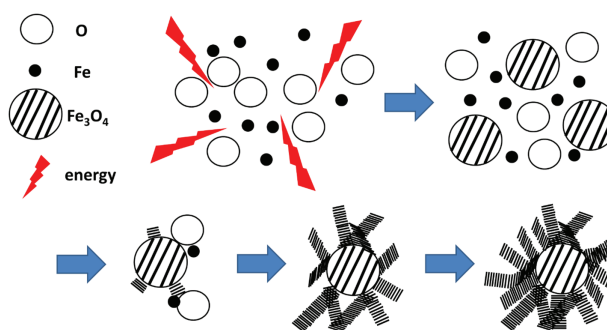


Figure 14. The sketch for the synthesis process and growth mechanism of Fe₃O₄ MNPs.

planes in the surface of the nucleus, other nuclei were stacked in the specific order decided by the planes in the surface of the nucleus. Therefore, the TEM images show the particles being demonstrated in a unidirectional extension and criss-cross crystal pattern. It is expected that such highly porous Fe₃O₄ nanoparticles can be applied for magnetic resonance imaging and therapeutic applications.⁴⁶

4. CONCLUSION

This work demonstrates a facile and eco-friendly microwave-assisted solvothermal method to produce highly porous Fe₃O₄ magnetic nanoparticles (MNPs) with a unidirectional extension crystal pattern. The particles become stable iron(III) oxide after a 60-min reaction when the temperature is fixed at 200 °C. The Fe₃O₄ nanoparticles usually show superparamagnetic properties, which reach their highest saturation magnetization of 30 emu/g for the sample prepared at 60 min. Except for XRD patterns, the XPS results also confirm that the synthesized particles are Fe₃O₄. The SEM images indicate that a reaction time over 60 min makes the reaction complete and the shape of the particles is much closer to being spherical with a particle size of 100–150 nm. The TEM bright field images indicate that numerous microcracks appear at the surface of the Fe₃O₄ particle, whereas the TEM dark field images show that the microcracks are caused by the agglomeration of many 2–6 nm Fe₃O₄ particles. These MNPs grow toward the same direction, which may be provided by the nuclei. Hence, the synthesized MNPs present porous microstructures, which yield 3 times larger surface area than commercially-available products.

For the mechanism to fabricate porous Fe₃O₄ nanoparticles, the reductant ethylene glycol reduces iron(III) chloride through absorbing the microwave energy at the beginning. The Fe₃O₄ nuclei are then formed and gotten together to decrease the surface energy. The nuclei with different crystal planes are stacked in the specific order decided by the planes in the surface of the nucleus. Hence, the particles are presented in the form of microcracks by TEM images. The present work unveils more information in the fabrication of Fe₃O₄ nanoparticles with

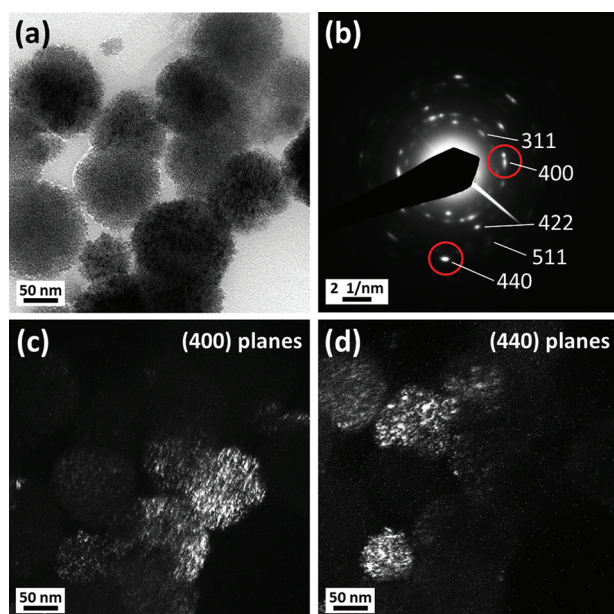


Figure 13. (a) The bright-field TEM images of the MNPs reacted at 200 °C for 60 min, (b) the electron diffraction pattern of the MNPs in (a). (c and d) Are the dark-field TEM images of selective beam sources of (400) and (440) in (b), respectively.

a comparatively high specific surface area. We hope that this research is beneficial to further development and applications of Fe₃O₄ nanoparticles.

Acknowledgments: Financial support for this work through grants from the Chang Gung Medical Foundation, Taiwan (No. CMRPD2E0072) and the Ministry of Science and Technology, Taiwan (No. MOST106-2221-E-155-015) is gratefully appreciated. The authors also thank the Microscope Core Laboratory of Chang Gung Memorial Hospital, Linkou, Taiwan for technical assistance on the FE-SEM and TEM measurements of the prepared samples.

References and Notes

1. L. Yu, J. D. Chen, Z. Liang, W. C. Xu, L. M. Chen, and D. Q. Ye, *Sep. Purif. Technol.* 171, 80 (2016).
2. S. X. Zhang, X. L. Zhao, H. Y. Niu, Y. L. Shi, Y. Q. Cai, and G. B. Jiang, *J. Hazard. Mater.* 167, 560 (2009).
3. S. Y. Bao, L. H. Tang, K. Li, P. Ning, J. H. Peng, H. B. Guo, T. T. Zhu, and Y. Liu, *J. Colloid Interface Sci.* 462, 235 (2016).
4. Y. L. Qin, M. C. Long, B. H. Tan, and B. X. Zhou, *Nano-Micro Lett.* 6, 125 (2014).
5. B. B. Lahiri, T. Muthukumar, and J. Philip, *J. Magn. Magn. Mater.* 407, 101 (2016).
6. J. A. Lopez, F. González, F. A. Bonilla, G. Zambrano, and M. E. Gómez, *Rev. Latinoam. Metal. Mater.* 30, 60 (2010).
7. F. Yazdani, B. Fattahi, and N. Azizi, *J. Magn. Magn. Mater.* 406, 207 (2016).
8. A. H. Rezayan, M. Mousavi, S. Kheirjou, G. Amoabediny, M. S. Ardestani, and J. Mohammadnejad, *J. Magn. Magn. Mater.* 420, 210 (2016).
9. Y. W. Jun, Y. M. Huh, J. S. Choi, J. H. Lee, H. T. Song, S. Sungjun, S. Yoon, K. S. Kim, J. S. Shin, J. S. Suh, and J. Cheon, *J. Am. Chem. Soc.* 127, 5732 (2005).
10. R. Tarasi, M. Khoobi, H. Niknejad, A. Ramazani, L. Mamani, S. Bahadorikhahali, and A. Shafiee, *J. Magn. Magn. Mater.* 417, 451 (2016).
11. D. Dorniani, M. Z. B. Hussein, A. U. Kura, S. Fakurazi, A. H. Shaari, and Z. Ahmad, *Int. J. Nanomed.* 7, 5745 (2012).
12. G. F. Goya, E. Lima, A. D. Arelaro, T. Torres, H. R. Rechenberg, L. Rossi, C. Marquina, and M. R. Ibarra, *IEEE Trans. Magn.* 44, 4444 (2013).
13. R. Ghosh, L. Pradhan, Y. P. Devi, S. S. Meena, R. Tewari, A. Kumar, S. Sharm, N. S. Gajbhiye, R. K. Vatsa, B. N. Pandey, and R. S. Ningthoujam, *J. Mater. Chem.* 21, 13388 (2011).
14. Q. L. Jiang, S. W. Zheng, R. Y. Hong, S. M. Deng, L. Guo, R. L. Hu, B. Gao, M. Huang, L. F. Cheng, G. H. Liu, and Y. Q. Wang, *Appl. Surface Sci.* 307, 224 (2014).
15. J. C. Apesteguy, G. V. Kurlyandskaya, J. P. de Celis, A. P. Safronov, and N. N. Schegoleva, *Mater. Chem. Phys.* 161, 243 (2015).
16. N. D. Kandpal, N. Sah, R. Joshi, and J. Prasad, *J. Sci. Ind. Res.* 73, 87 (2014).
17. D. Maity, S. G. Choo, J. B. Yi, J. Ding, J. M. Xue, *J. Magn. Magn. Mater.* 321, 1256 (2009).
18. V. Patsula, L. Kosinova, M. Lovric, L. F. Hamzic, M. Rabyk, R. Konefal, A. Paruzel, M. Slouf, V. Herynek, S. Gajovic, and D. Horak, *ACS Appl. Mater. Interfaces* 8, 7238 (2016).
19. C. Okoli, M. Sanchez-Dominguez, M. Boutonnet, S. Jaras, C. Civera, C. Solans, and G. R. Kuttuva, *Langmuir* 32, 8479 (2012).
20. E. Iglesias-Silva, J. Rivas, L. M. L. Isidro, and M. A. Lopez-Quintela, *J. Non-Cryst. Solids* 353, 829 (2007).
21. X. D. Liu, H. Chen, S. S. Liu, L. Q. Ye, and Y. P. Li, *Mater. Res. Bull.* 62, 217 (2015).
22. S. B. Ni, X. H. Wang, G. Zhou, F. Yang, J. M. Wang, Q. Wang, and D. Y. He, *Mater. Lett.* 63, 2701 (2009).
23. X. H. Sun, C. M. Zheng, F. X. Zhang, Y. L. Yang, G. J. Wu, A. M. Yu, and N. J. Guan, *J. Phys. Chem.* 113, 16002 (2009).
24. H. S. Chae, S. H. Piao, and H. J. Choi, *J. Ind. Eng. Chem.* 29, 1289 (2015).
25. W. Zhang, F. L. Shen, and R. Y. Hong, *Particuology* 9, 179 (2011).
26. O. M. Lemine, K. Omri, B. Zhang, L. El Mir, M. Sajjeddine, A. Alyamani, and M. Bououdina, *Superlatt. Microstruct.* 52, 793 (2012).
27. J. Xu, H. B. Yang, W. Y. Fu, K. Du, Y. M. Sui, J. J. Chen, Y. Zeng, M. H. Li, and G. T. Zou, *J. Magn. Magn. Mater.* 309, 307 (2007).
28. G. Marchegiani, P. Imperatori, A. Mari, L. Pilloni, A. Chiolerio, P. Allia, P. Tiberto, and L. Suber, *Ultrason. Sonochem.* 19, 877 (2012).
29. R. A. Mukh-Qasem and A. Gedanken, *J. Colloid Interface Sci.* 284, 489 (2005).
30. R. Vijayakumar, Yu. Koltypin, I. Felner, and A. Gedanken, *Mater. Sci. Eng. A* 286, 101 (2000).
31. J. F. de Carvalho, S. N. de Medeiros, M. A. Morales, A. L. Dantas, and A. S. Carriço, *Appl. Surface Sci.* 275, 84 (2013).
32. G. F. Goya, *Solid State Comm.* 130, 783 (2004).
33. W. W. Wang, Y. J. Zhu, and M. L. Ruan, *J. Nanoparticle Res.* 9, 419 (2007).
34. Z. Kozakova, P. Bazant, M. Machovsky, V. Babayan, and I. Kuritka, *Acta Physica Polonica A* 118, 948 (2010).
35. P. Coppola, F. G. da Silva, G. Gomide, F. L. O. Paula, A. F. C. Campos, R. Perzynski, C. Kern, J. Depeyrot, and R. Aquino, *J. Nanoparticle Res.* 18, 138 (2016).
36. H. S. Chae, S. H. Piao, and H. J. Choi, *J. Ind. Eng. Chem.* 29, 129 (2015).
37. H. Tju, A. Taufik, and R. Saleh, *J. Phys.: Conference Series* 710, 012005 (2016).
38. B. Ankamwar, T. C. Lai, J. H. Huang, R. S. Liu, M. Hsiao, C. H. Chen, and Y. K. Hwu, *Nanotechnology* 21, 075102 (2010).
39. T. K. Jain, M. K. Reddy, M. A. Morales, D. L. Leslie-Pelecky, and V. Labhasetwar, *Mol. Pharm.* 5, 316 (2008).
40. J. L. Corchero and A. Villaverde, *Trends Biotechnol.* 27, 468 (2009).
41. A. S. Lubbe, C. Bergemann, W. Huhnt, T. Fricke, H. Riess, J. W. Brock, and D. Huhn, *Cancer Res.* 56, 4694 (1996).
42. Z. Mei, A. Dhanale, A. Gangaharan, D. K. Sardar, and L. Tang, *Talanta* 151, 23 (2016).
43. Y. L. Wang, Y. J. Sun, H. C. Dai, P. J. Ni, S. Jiang, W. D. Lu, Z. Li, and Z. Li, *Sensors Actuators B: Chem.* 236, 621 (2016).
44. X. S. Wang, H. Huang, G. Q. Li, Y. Liu, J. L. Huang, and D. P. Yang, *Nano. Res. Lett.* 9, 249 (2014).
45. J. H. Ma, L. L. Wang, Y. L. Wu, X. S. Dong, Q. L. Ma, C. Qiao, Q. F. Zhang, and J. L. Zhang, *Mater. Trans.* 55, 1900 (2014).
46. S. H. Xuan, F. Wang, J. M. Y. Lai, K. W. Y. Sham, Y. X. J. Wang, S. F. Lee, J. C. Yu, C. H. K. Cheng, and K. C. F. Leung, *ACS Appl. Mater. Interfaces* 3, 237 (2011).
47. L. Wang, H. M. Ji, S. S. Wang, L. J. Kong, X. F. Jiang, and G. Yang, *Nanoscale* 5, 3793 (2013).
48. M. Y. Ho, P. S. Khiew, D. Isa, T. K. Tan, W. S. Chiu, C. H. Chia, M. A. A. Hamis, and R. Shamsudin, *Sains Malaysiana* 43, 885 (2014).
49. E. P. Barrett, L. G. Joyner, and P. P. Halenda, *J. Am. Chem. Soc.* 73, 373 (1951).
50. B. D. Cullity, *Element of X-ray Diffraction*, 2nd edn., Addison-Wesley, Canada (1978), p. 101.
51. S. Gota, E. Guiot, M. Henriot, and M. Gautier-Soyer, *Phys. Rev. B* 60, 14387 (1999).
52. C. Hui, C. M. Shen, T. Z. Yang, L. H. Bao, J. F. Tian, H. Ding, C. Li, and H. J. Gao, *J. Phys. Chem.* 112, 11336 (2008).

Received: 2 May 2018. Accepted: 17 December 2018.